Bulletin of Engineering Geology and the Environment (2023) 82:356
https://doi.org/10.1007/s10064-023-03378-y

ORIGINAL PAPER

Hydrochemistry process and microweathering behaviour of sandstone heritages in the Nankan Grotto, China: Insights from field micro-observations and water–rock interaction experiments

Xuening Zhang[1] · Sixiang Ling[1,2] · Xiyong Wu[1,2] · Fengrui Wang[3] · Jie Wang[3] · Qiang Teng[1] · Jiawen Xie[1]

Received: 6 February 2023 / Accepted: 4 August 2023 / Published online: 19 August 2023

Abstract

Geochemical analyses of groundwater samples and water─rock interaction experiments were conducted to elucidate the hydrochemical process of the water─rock interactions in the Nankan mountainside. Additionally, the mineralogy and microstructure of field sandstone samples were analysed to explore the microweathering behaviour of minerals in the Nankan Grotto. The results indicated that the cations in the groundwater followed the concentration order of $Ca^{2+} > Mg^{2+} \approx Na^{+} >> K^{+}$, while the anion concentrations were in the order of $HCO_3^{-} >> NO_3^{-} > SO_4^{2-} \approx Cl^{-}$. The Piper, Gibbs, and ion correlation diagrams suggested that the groundwater was characterized as HCO_3-Ca type. Three stages, the calcite dissolution stage (Stage I), feldspar weathering stage (Stage II), and faint─weathering stage (Stage III) were observed in the water─rock interaction experiments. Based on microscopic petrographical analysis, the dissolution of calcite released bulk Ca^{2+} and HCO_3^{-}, and this was the primary hydrochemical process that accounted for the HCO_3-Ca type groundwater. The weathering of biotite to chlorite-(Mg) introduced Mg^{2+} and K^{+}. The weathering of albite and plagioclase-TIMA to sericite or other clay minerals released Na^{+} and Ca^{2+} into the solution. Slight weathering of K-feldspar released minor amounts of K^{+} into the solution. The abovementioned weathering processes resulted in the poor cementation and loose microstructure of the sandstone, leading to the macroscopic deterioration of the sandstone heritage site. Our research revealed the deterioration mechanisms of the sandstone in the Nankan Grotto, which paves the way for the subsequent conservation of sandstone heritage sites.

Keywords Sandstone heritage · Microweathering · Hydrochemistry · Deterioration mechanism · Water─rock interaction

---

✉ Sixiang Ling
lingsx@swjtu.edu.cn

Xuening Zhang
zxning@my.swjtu.edu.cn

Xiyong Wu
wuxiyong@swjtu.edu.cn

Fengrui Wang
651704456@qq.com

Jie Wang
695183539@qq.com

Qiang Teng
2020201366@my.swjtu.edu.cn

Jiawen Xie
157981424@my.swjtu.edu.cn

[1] Faculty of Geosciences and Environmental Engineering, Southwest Jiaotong University, 611756 Chengdu, Sichuan Province, People's Republic of China

[2] MOE Key Laboratory of High-Speed Railway Engineering, Southwest Jiaotong University, Chengdu, Sichuan Province 610031, People's Republic of China

[3] Northwest Research Institute Co., Ltd. of China Railway Engineering Corporation, Lanzhou, Gansu Province 730099, People's Republic of China

Introduction

Stone monuments reflect the diverse artistic, historical, and scientific achievements of humans and are often closely connected with natural landforms (Bonomo et al. 2020). Sandstone is a common sedimentary lithology used for monuments worldwide, and it develops striking relief features in heritage sites (Siegesmund and Snethlage 2011; Sun and Zhang 2019). The sandstone of heritage sites is generally dense and hard due to excellent cementation in the calcareous or siliceous matrix (Sun and Zhang 2019). However, sandstone monuments have undergone various degrees of degradation over long geological timescales due to the combined influences of petrography, petrophysical properties, the environment, and anthropogenic disturbances (André et al. 2012; Germinario et al. 2020; Hatır et al. 2018; Paradise 1995; Sabbioni and Zappia 1992; Zammit and Cassar 2015).

The weathering mechanisms identified in previous studies of sandstone heritage sites can be classified into those caused by geological factors and those caused by environmental factors. Environmental factors have been extensively addressed in studies on weathering mechanisms, including salt-induced decay (Cardell et al. 2003; Hosono et al. 2006; Siedel 2018), biological or microbiological damage to monuments (Levett et al. 2020; Liu et al. 2020; Xu et al. 2018), and air pollution (Cardell et al. 2003; Grøntoft and Cassar 2020; Sabbioni and Zappia 1992; Williams and Robinson 2000). Notably, research on the environmental factors leading to sandstone decay has been greatly concerned with the chemical and mechanical effects of infiltrating water (Germinario and Oguchi 2022; Yan et al. 2022). It is very important to further comprehend the weathering mechanisms driven by water−rock interactions in sandstone strata to provide appropriate protections for sandstone heritages. However, the microscopic weathering processes that are driven by water−rock interactions in sandstone heritage sites have not been thoroughly studied. Previous studies have mainly focused on conducting accelerated weathering experiments to ascertain the physical–mechanical properties of sandstone, such as its weight, porosity, water absorption characteristics, ultrasonic wave velocity, hardness, and compressive/tensile stress before and after reactions with chemical solutions (Dursun and Topal 2019; Rothert et al. 2007; Ruedrich and Siegesmund 2007; Sun and Zhang 2019; Yu and Oguchi 2010). A better understanding of the microscopic behaviour of minerals and major elements involved in water–rock interactions can promote an understanding of the microweathering process and deterioration mechanisms of sandstone heritage sites.

The Nankan Grotto is an exquisite sandstone monument representing Buddhist and Taoist grotto art from the Sui and Tang dynasties, and it has undergone severe weathering over more than 1300 years. The typical deterioration patterns and processes of the sandstone in the Nankan Grotto have been preliminarily explored from the perspective of micropetrography, and we noticed that infiltrated water, including rainwater and groundwater, was an indisputable factor in the sandstone deterioration process. However, the detailed microscopic process of water−rock interactions in the Nankan Grotto is still unclear. Therefore, we further collected groundwater and rainwater for hydrochemical analysis, and collected fresh and weathered solid samples for mineralogical analysis from locations that were frequently exposed to rainfall or groundwater. We also conducted two water−rock interaction experiments to investigate potential geochemical interactions. The main objectives of this study were (i) to analyse the hydrochemical characteristics and trace the sources of major ions in the groundwater, (ii) to investigate the microweathering behaviour of minerals and elements in the sandstone of the Nankan Grotto, and (iii) to elucidate the deterioration mechanisms of sandstone caused by water−rock interactions in the Nankan Grotto. This study provides new evidence for a better understanding of the weathering processes and deterioration mechanisms of sandstone grotto heritage sites.

Study site

The Nankan Grotto is located at the Nankan mountainside in Bazhong city, Sichuan Province (Fig. 1). The cave of the Nankan Grotto was dated to the Sui dynasty and was mainly engraved in the Tang dynasty. It is a well-preserved large-scale grotto in a sandstone cliff, and it was included in the third batch of major historical and cultural sites at the national level by the State Council in 1988. Bazhong city features a subtropical humid mountain climate that is controlled by the Asian monsoons. The average annual temperature and precipitation in the study area are approximately 16 °C and 1117.2 mm, respectively (http://www.cnbz.gov.cn). The annual relative humidity varies from 64 to 84%.

The strata exposed in the Nankan Mountain area consists of the Cretaceous Cangxi Formation (K_1c), Cretaceous Bailong Formation (K_1b), and Quaternary sediments (Fig. 1). The Cangxi and Bailong Formations are subhorizontal strata dominated by siliceous and calcareous sandstone. The structure of Nankan Mountain is a gentle syncline (Fig. 1). Groundwater flows from the axis to the limbs of Nankan Mountain. The recharge for groundwater is derived from the infiltration of precipitation, and the groundwater discharges as cold springs. Bedrock fissure water is a significant component of the groundwater in the Nankan Mountain area. The groundwater in the study area is mainly unconfined water.

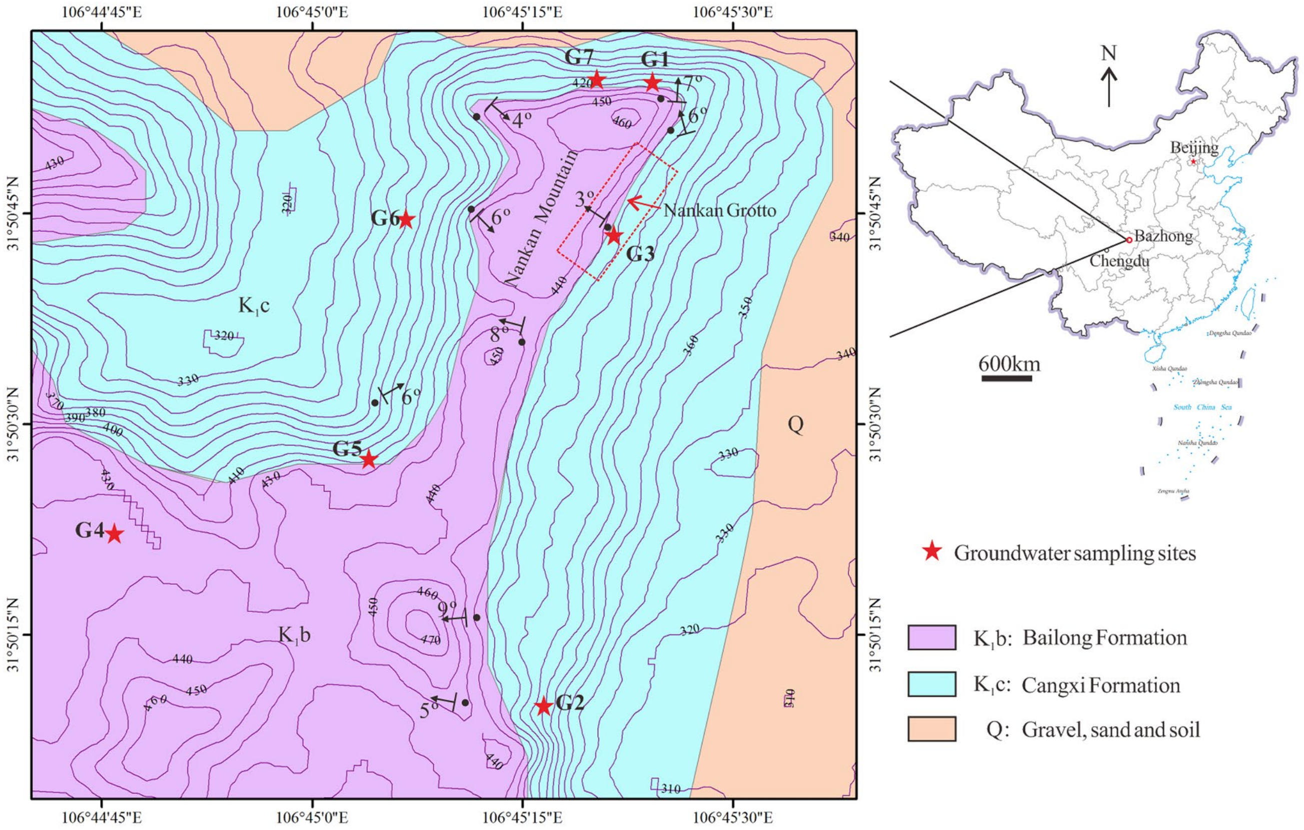

Fig. 1 Topographical and geological map of the study area around the Nankan Grotto heritage site and groundwater sampling sites (G1-G7)

Methods

Field water sample collection and analysis

Groundwater samples were collected from 7 sites around the Nankan mountainside on April 26–27, 2022 (Fig. 1). Samples G1, G2, G5, and G7 were from cold spring water. The sampling sites of G3, G4, and G6 were existing boreholes with sampling depths of 5–10 m. Groundwater in the boreholes was pumped for more than 20 min to remove the stagnant water in the pipeline and sampled until the in situ parameters (pH, electrical conductance (EC)) of pumped-out groundwater were stable. All of the groundwater samples were shallow phreatic groundwater. Groundwater samples G1, G3, G5, and G7 were collected from the boundary of the Bailong and Cangxi Formations. Samples G2 and G6 were collected from the Cangxi Formation. Sample G4 was collected from the Bailong Formation. Seven groundwater samples were collected from different formations to explore the differences in hydrochemical characteristics. One rainwater sample (R1) was collected at the Nankan Grotto on April 27, 2022, using an automatic rainwater collector (GH-200, China).

The water samples were filtered through 0.45 μm nylon filters at each site after collection and then separated into two aliquots. One was stored in a prerinsed polyethylene bottle for measuring anions. The other was stored in a precleaned polyethylene bottle and acidified with ultrapurified HNO_3 to $pH < 2$ for measuring cations. All the samples were stored in potable incubators at a temperature of 4 °C and transported to the laboratory within a week. The pH, EC, and total dissolved solids (TDS) of the samples were measured in situ using a portable multimeter device (HANNA HI98129, Italy). Major cations (Ca^{2+}, Mg^{2+}, Na^{+}, K^{+}) were determined by inductively coupled plasma−optical emission spectrometry (ICP−OES, Perkin Elmer 8300). Major anions (Cl^{-}, SO_4^{2-}, NO_3^{-}) were measured using ion chromatography (IC, Dionex ICS-1100, Thermo Fisher Scientific Inc., USA). HCO_3^{-} was detected by acid−base titration in the laboratory. Measurements were carried out on standard and parallel samples, and the relative deviation (RD) and relative error (RE) of the ICP−OES and IC measurements were less than 5%. The charge balance error (%CBE) was calculated to assess the accuracy of all chemical analyses of water samples. The %CBE was computed using the following equation:

$$\%CBE = \frac{\sum Cations - \sum Anions}{\sum Cations + \sum Anions} \times 100\% \quad (1)$$

with total concentrations of cations ($Ca^{2+} + Mg^{2+} + Na^{+} + K^{+}$) and the total concentrations of anions ($HCO_3^{-} + Cl^{-} + SO_4^{2-} + NO_3^{-}$). The %CBE results show that all water samples in the Nankan area are within the permissible limit of ± 10% (Adimalla et al. 2020a).

Field solid sample collection and analysis

The sandstone of the Nankan Grotto has a reddish colour and belongs to the Lower Cretaceous Bailong Formation. Three parallel deposit sequences are presented, named Bedding-3, Bedding-2, and Bedding-1, from the top of the ground surface to the bottom of the grotto (Fig. 2). Solid samples were collected from locations that were exposed to rainfall or seepage. Samples SW1–3 were weathered sandstone samples from Bedding-1 (Fig. 2a–b). Samples SW4 and SW5 were weathered sandstone samples from Bedding-2 and Bedding-3, respectively (Fig. 2c). Samples SF1 and SF2 were fresh sandstone samples from Bedding-1 and Bedding-3, respectively.

After collection, the solid samples were dried in an oven at 65 °C for 24 h in the laboratory. Then, the samples were pulverized to silt-sized particles using an XQM-0.4A ball mill with a zirconia ball. The pulverized samples were ground using an agate mortar and a pestle, and then passed through a 200-mesh sieve (< 75 μm) before laboratory analysis. The mineralogical compositions of the powdered whole rock samples were determined via X-ray diffraction (XRD), with a Bruker D8 DISCOVER diffractometer (Germany) equipped with Cu-Kα radiation ($\lambda = 1.54059$ Å) operated at 40 kV and 40 mA. The XRD patterns were recorded at 2θ angles from 5° to 45° with a step size of 0.02°/sec. The mineral concentrations were quantified using whole pattern fitting and Rietveld refinement. The relative standard deviation (RSD) was less than 10%, and the lowest detection limit was 0.1 wt.%.

The unpolished samples (SF1, SW2–4) were coated with platinum (Emitech SC7620 sputter coater) prior to observation. The microstructure of the above samples was observed via a tungsten filament scanning electron microscope (SEM, JSM-IT500, Japan) with an accelerating voltage of 15 kV. The elemental compositions of the selected mineral grains were analysed via an Oxford ULTIM Max 40 EDS system.

Prior to observation, the sandstone samples were polished using a polishing machine (UNIPOL-1200 M) to obtain flat surfaces and then coated with carbon. Backscattered electron (BSE) images were obtained by SEM at an accelerating voltage of 15–25 kV. EDS was used to identify the mineralogical compositions of the observed grains. The compositional maps were obtained using the TIMA system.

The morphological and textural alteration of minerals and elemental composition were visualized by a TESCAN Integrated Mineral Analyser (TIMA, Czech Republic). TIMA is an integrated system equipped with a field emission scanning electron microscope (TESCAN MIRA-3, Czech Republic), four energy dispersive X-ray spectroscopy (EDS, EDAX Element 30), and the corresponding software for data analysis. The TIMA instrument was equipped with MAC standard 12,925 to automatically calibrate the instrument before each chemical analysis. MAC standard 12,925 is an authoritative mineral reference material and was provided by the instrument manufacturer (Czech Republic). The current and backscattered electron (BSE) signal intensity were calibrated on a platinum Faraday cup using the automated procedure. The calibration set point was 600 kcps. The EDS performance was checked using a manganese standard. In addition, 10 standard mineral samples, which were made from high purity materials, were used to calibrate the TIMA instrument each quarter. Therefore, quantitative chemical analysis is accurate and reliable.

In XRD pattern identification, plagioclase cannot be subdivided and includes albite, oligoclase, andesine,

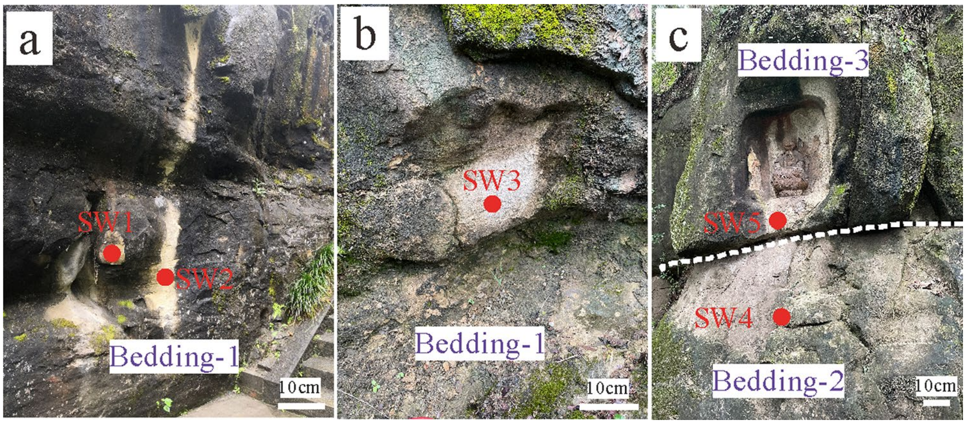

Fig. 2 Sampling sites of the sandstone samples. **a** Sampling sites of weathered samples SW1–2. **b** Sampling site of weathered sample SW3. **c** Sampling sites of weathered samples SW4–5

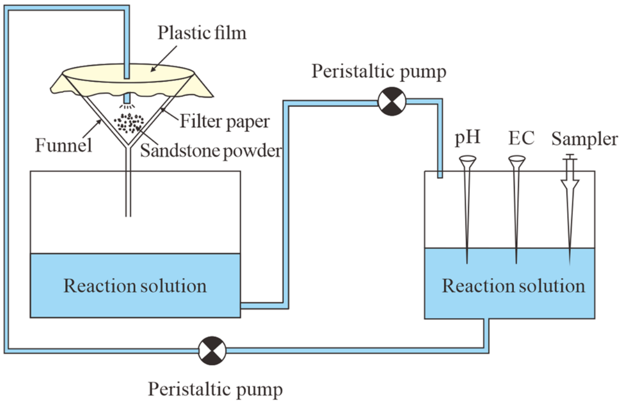

Fig. 3 Schematic diagram showing the cyclic water–rock interaction experiment

labradorite, bytownite, and anorthite. However, albite can be clearly identified from the TIMA system. Therefore, the plagioclase symbol in the TIMA system included only oligoclase, andesine, labradorite, bytownite, and anorthite. To differentiate between the plagioclase identified from the XRD and TIMA techniques, plagioclase from the XRD analysis is labelled plagioclase-XRD and that from the TIMA analysis is labelled plagioclase-TIMA.

Water–rock interaction experiments

A cyclic water–rock interaction experiment for sandstone was designed to elucidate the microscopic weathering mechanism of the sandstone in the Nankan Grotto (Fig. 3). Fresh sandstone sample powders (< 150 µm, 50 g) were placed in a funnel containing filter paper with pore diameters < 6–8 µm. Then, 4 L deionized water was slowly injected into the funnel to react with the sandstone powders, so the solid:water weight ratio was 1:80. The funnel was sealed with a polyethylene plastic film to prevent evaporation. After each cycle, the interacting solution was collected in a polyethylene tank for pH/conductivity/TDS tests (HANNA HI98129, Italy), and then reinjected into the funnel for the next cycle (Fig. 3). After cycles 10, 20, 30, 40, 50, and 60, 5 mL of reaction solution was sampled and acidified with ultra-purified HNO_3 for the ion concentration test (ICP–OES, Perkin Elmer 8300), and here, the impact of the next reaction cycle was neglected (Sun et al. 2021). The total duration of the experiment was 60 days.

To explore the whole process of sandstone weathering in the Nankan Grotto, an additional acid-accelerated weathering experiment was designed. In this experiment, HNO_3 solution was used to provide H^+ without inducing the formation of crystalline salts. In each cycle, 0.25 L of the HNO_3 solution ($pH = 3$) was poured into 40 g of fresh sandstone powders (< 150 µm), which were placed on filter paper with pore diameters < 6–8 µm in a funnel. The solid:water weight ratio was 16:100. The funnel was sealed with a polyethylene plastic film to prevent evaporation. The interacting solution was completely collected at the end of each cycle and a new 0.25 L of HNO_3 solution ($pH = 3$) was decanted into the funnel for the next cycle. At the end of each acid water– rock interaction cycle, the interacting solution was tested using a calibrated pH/conductivity/TDS meter (HANNA HI98129, Italy). After cycles 1, 9, 19, 29, 39, 51, and 67, 5 mL of reaction solution was sampled and acidified with ultra-purified HNO_3 for the ion concentration test (ICP–OES, Perkin Elmer 8300). The total duration of the experiment was 67 days. The initial physicochemical characteristics of the two experiments are shown in Table 1.

Results

pH, EC, TDS values and ionic concentrations of the field water samples

In the groundwater samples (G1–G7), the pH values ranged from 7.84 to 8.15, showing slightly alkaline characteristics (Table 2). The EC and TDS values were in the range of 403–557 µs/cm and 201–278 mg/L, respectively. The concentration of major cations was in the order $Ca^{2+} > Mg^{2+} \approx Na^+ >> K^+$. The abundance of major anions was in the following order: $HCO_3^- >> NO_3^- > SO_4^{2-} \approx Cl^-$. Even though groundwater samples G1-G7 were collected from different formations, the hydrochemical differences between them were not obvious. Notably, sample G4, which was

Table 1 Physicochemical characteristics for the water–rock interaction experiments

Name	Powder grain size	Solid:water weight ratio	Reactive solution	Experimental mode	Duration (days)
Cyclic water–rock interaction experiment	< 150 µm	1:80	deionized water	cyclic experiment	60 d
Acid-accelerated weathering experiment	< 150 µm	16:100	$pH = 3$ HNO_3 solution	single experiment for each cycle	67 d

Table 2 pH, EC, TDS values and ionic concentrations of water samples.

Description	Sample	pH	EC (µs/cm)	TDS (mg/L)	K$^+$ (mg/L)	Na$^+$ (mg/L)	Ca^{2+} (mg/L)	Mg^{2+} (mg/L)	Cl$^-$ (mg/L)	SO$_4^{2-}$ (mg/L)	NO$_3^-$ (mg/L)	HCO$_3^-$ (mg/L)
Groundwater	G1	8.15	557	278	0.56	19.70	159.90	25.06	20.35	35.93	22.83	245.90
	G2	8.0	505	252	1.16	20.57	141.30	22.04	31.98	36.83	42.58	212.30
	G3	7.84	472	236	1.63	12.96	113.10	16.90	6.90	9.34	23.57	257.00
	G4	8.06	519	259	10.24	19.04	121.75	12.55	32.73	12.51	93.91	212.30
	G5	8.15	481	240	1.32	30.31	170.40	33.26	18.85	22.19	40.80	257.00
	G6	8.06	403	201	1.64	20.18	124.50	16.99	6.02	14.50	28.03	201.20
	G7	7.91	526	263	1.45	25.54	131.20	21.62	20.17	20.72	30.38	212.30
Rainwater	R1	6.84	17	8	0.75	0.73	16.61	2.44	0.52	0.46	4.46	40.30

collected from the Bailong Formation, showed the highest concentrations of NO$_3^-$, Cl$^-$, and K$^+$. Sample G5, which was collected from the boundary of the Bailong and Cangxi Formations, showed the highest concentrations of Na$^+$, Ca^{2+}, Mg^{2+}, and HCO$_3^-$. The concentrations of Ca^{2+}, Mg^{2+}, Na$^+$, K$^+$, NO$_3^-$, and Cl$^-$ in the Nankan area were in ranges similar to those in the Nanchong area (Zhang et al. 2021), which is adjacent to Bazhong city and has the Cretaceous Cangxi Formation (K$_1$c) and Bailong Formation (K$_1$b). However, the concentrations of HCO$_3^-$ and SO$_4^{2-}$ in the Nankan area were lower than those in the Nanchong area.

In rainwater sample R1, the EC and TDS values and ion concentrations were much lower than those in the groundwater samples (Table 2). The pH, EC and TDS values were 6.84, 17 µs/cm and 8 mg/L, respectively.

Mineralogy of the sandstone

The XRD analysis results of the solid sandstone samples are shown in Table 3 and Fig. S1. Here, we used plagioclase-XRD as the symbol for XRD analysis, and it includes albite, oligoclase, andesine, labradorite, bytownite, and anorthite. In the fresh sandstone samples (SF1–2), the quartz concentrations were the highest (63.0–66.6 wt.%), followed by plagioclase-XRD (12.3–20.1 wt.%), clay minerals (6.7–9.8 wt.%), K-feldspar (4.2–5.4 wt.%), calcite (3.6–4.9 wt.%), ankerite (0.7–1.3 wt.%), and hematite (0.4–1.0 wt.%) concentrations.

In the weathered sandstone samples (SW1–5), the quartz concentrations were the highest (68.0–72.6 wt.%), followed by plagioclase-XRD (7.8–13.7 wt.%), clay minerals (6.4–7.9 wt.%), K-feldspar (3.8–8.7 wt.%), and calcite (2.8–8.5 wt.%) concentrations. Hematite and ankerite were observed only in sample SW3, with concentrations of 0.5 wt.% and 0.7 wt.%, respectively.

Microscopic observations for sandstone

The SEM micrographs of the unpolished samples (SF1, SW2–4) are presented in Fig. 4. In fresh sample SF1, the microstructures were intact (Fig. 4a). The mineral surfaces were smooth, and the mineral grains were tightly cemented (Fig. 4a). As the weathering degree increased, the mineral grains were corroded and loosely cemented in weathered samples SW2 and SW3. Moreover, microcracks were widely spread along the mineral boundaries (Fig. 4b, c). Mineral fragments were loosely scattered on the mineral surfaces or in the gaps between the minerals in sample SW2 (Fig. 4b). Crystals of secondary calcite were observed to have precipitated

Table 3 Mineral concentrations (wt.%) of the solid samples obtained via XRD

Description	Bedding	Sample	Quartz	Plagioclase-XRD	K-feldspar	Calcite	Hematite	Ankerite	Clay mineral
Fresh	Bedding-1	SF1	63.0	20.1	4.2	4.9	0.4	0.7	6.7
	Bedding-3	SF2	66.6	12.3	5.4	3.6	1.0	1.3	9.8
Weathered	Bedding-1	SW1	72.1	12.1	5.1	2.8	-	-	7.9
	Bedding-1	SW2	70.7	13.7	3.8	4.8	-	-	7.0
	Bedding-1	SW3	72.6	7.8	4.7	8.5	-	-	6.4
	Bedding-2	SW4	70.3	11.8	4.1	5.2	0.5	0.7	7.4
	Bedding-3	SW5	68.0	11.7	8.7	4.6	-	-	7.0

"-" indicates a concentration below the detection limit of 0.1 wt.%. The term "plagioclase-XRD" includes albite, oligoclase andesine, labradorite, bytownite, and anorthite

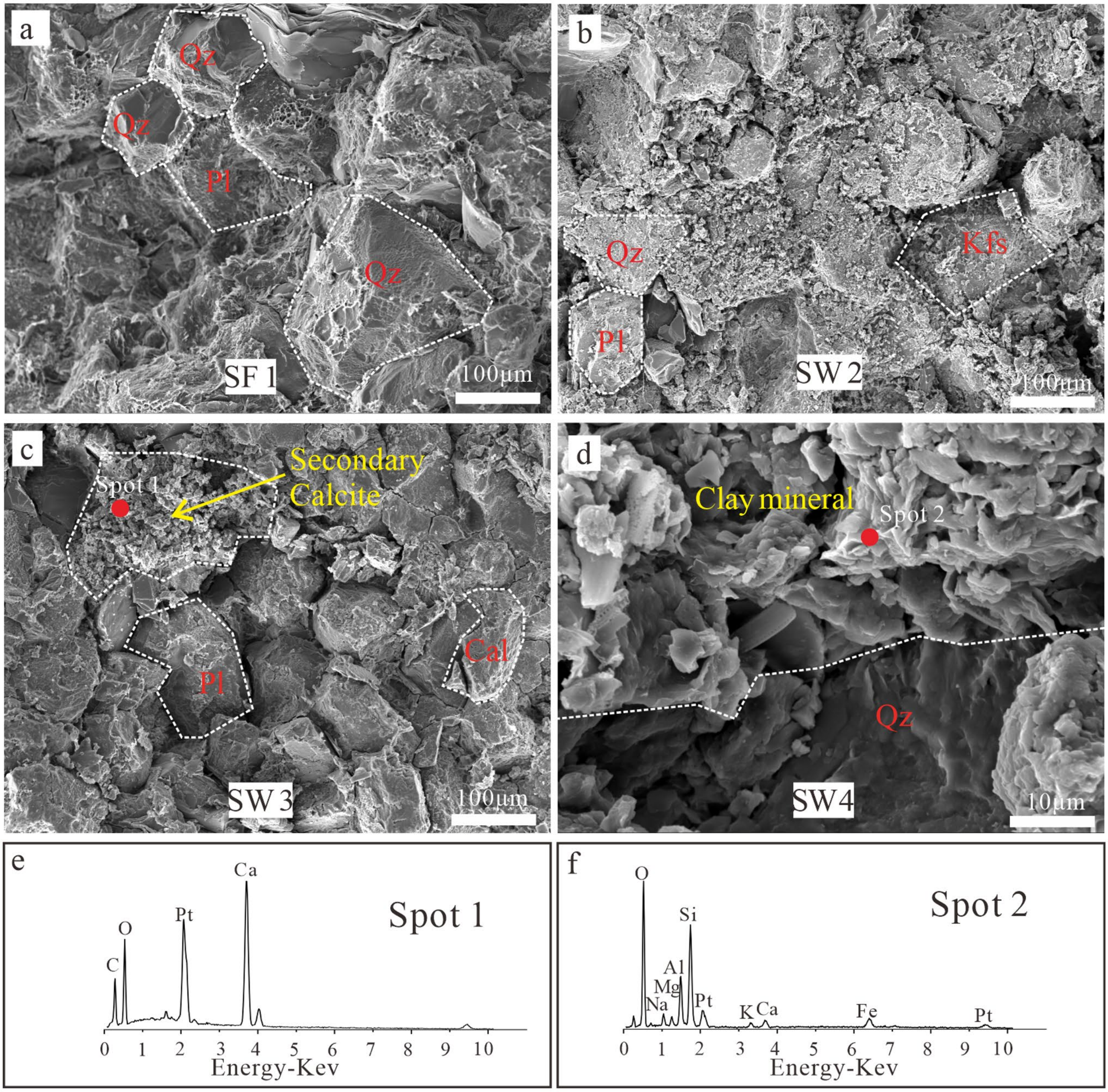

Fig. 4 SEM micrographs and representative EDS spectra of the unpolished samples (SF1, SW2–4). **a** SEM image of sample SF1. **b** SEM image of sample SW2. **c** SEM image of sample SW3. **d** SEM image of sample SW4. **e** EDS spectra of spot 1 in sample SW3. **F** EDS spectra of spot 2 in sample SW4. Qz = quartz, Pl = Plagioclase-XRD, Kfs = K-feldspar, Cal = calcite

on the mineral surfaces in sample SW3 and were grouped in small clusters (Fig. 4c, e). In weathered sample SW4, EDS point analysis indicated that lamellar clay minerals were attached to the skeleton mineral surfaces (Fig. 4d, f).

BSE micrographs of the weathered samples (SW1–5) are presented in Fig. 5. In the TIMA system, the symbol for plagioclase is plagioclase-TIMA, and it includes only oligoclase, andesine, labradorite, bytownite, and anorthite; albite can be identified in the TIMA system. In weathered samples SW1 and SW2, lamellar clay minerals were detected on the albite surface (Fig. 5a, c). Ca, Fe, Mg, and K were included within the clay mineral lattice (Fig. 5b, d). Microcracks were widely observed along the cleavage planes of calcite in sample SW3 (Fig. 5e–f), corresponding to the highest calcite concentration of any sample (Table 3). The albite displayed a rough surface, with some erosion pits and grooves on its

Fig. 5 BSE micrographs and representative EDS spectra of the weathered samples (SW1–5). **a**–**b** BSE image and EDS spectra of sample SW1. **c**–**d** BSE image and EDS spectra of sample SW2. **e**–**f** BSE image and EDS spectra of sample SW3. **g**–**h** BSE image and EDS spectra of sample SW4. **i**–**j** BSE image and EDS spectra of sample SW5

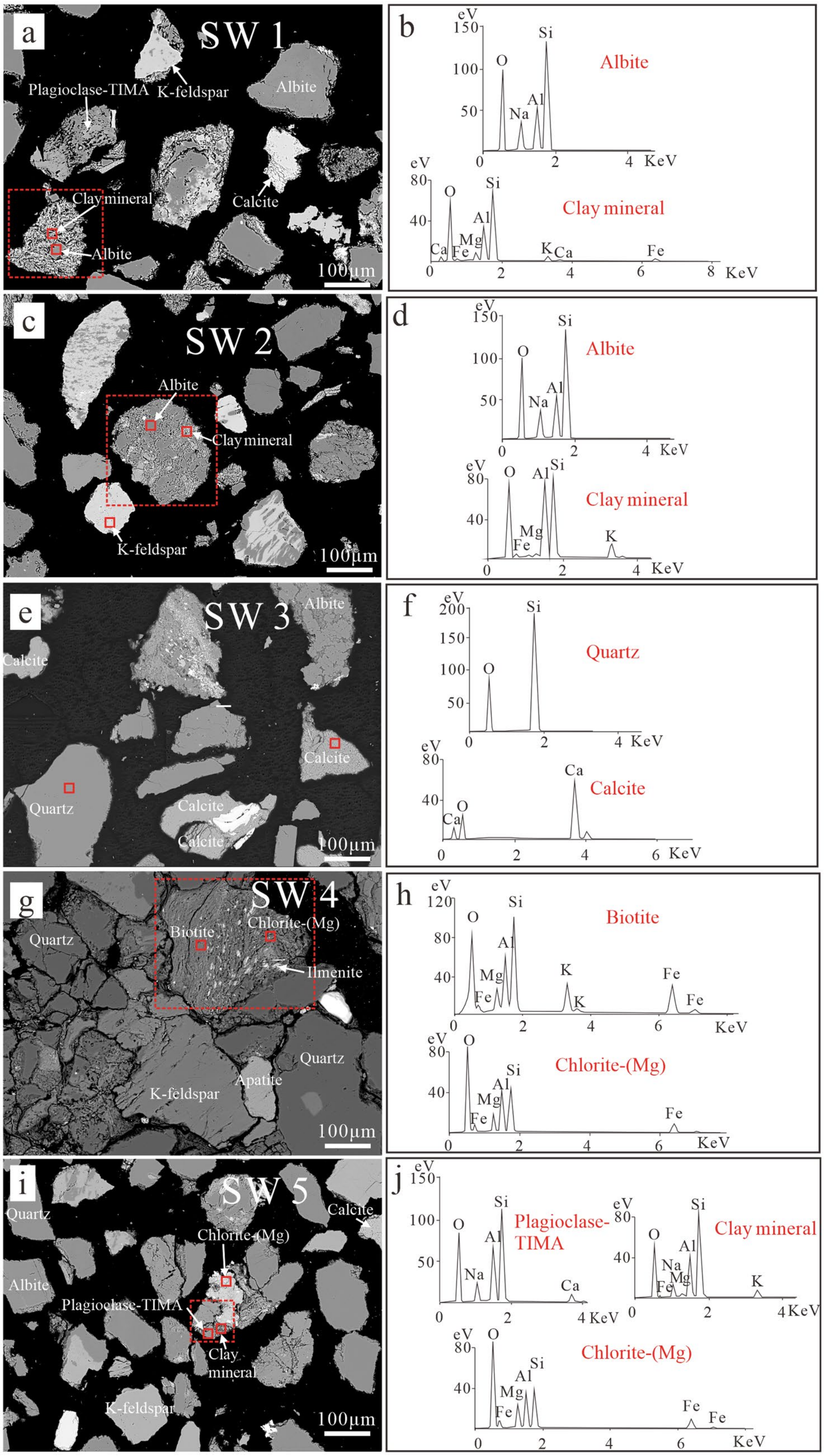

surface (Fig. 5e). In sample SW4, Fe^{2+} in biotite was altered to ilmenite, whereas the residue was altered to chlorite-(Mg) (Fig. 5g). In sample SW5, lamellar clay minerals were observed on the plagioclase-TIMA grain (Fig. 5i). Fe, K and Mg were included within the clay mineral lattice (Fig. 5j).

The BSE micrograph, mineral map, and element maps of fresh sample SF1 and weathered sample SW1 are shown in Fig. 6. In the fresh sample SF1, the minerals were tightly cemented by aluminosilicate materials, resulting in the intact microstructure of the sample (Fig. 6a–b). The mineral map shows abundant amounts of quartz, followed by albite, K-feldspar, plagioclase-TIMA, and calcite. In addition, minor amounts of biotite, muscovite, and chlorite were also observed in the mineral map but were not detected by XRD (Fig. 6b). K was mainly present in K-feldspar, muscovite, and biotite (Fig. 6c). Minor amounts of K were present in clay minerals. Fe was clustered in hematite, biotite, and chlorite (Fig. 6d). Mg was mainly enriched in chlorite and partly distributed in biotite (Fig. 6e).

In weathered sample SW1, the mineral margins were corroded into rough edges (Fig. 6f). Furthermore, microcracks were widely developed in quartz and feldspar (Fig. 6f). The mineral grains presented loose cementation, and the matrix dissolved to form pores as weathering proceeded (Fig. 6g). The most apparent change was the complete dissolution of calcite, which generated many macromouldic pores over 100 mm in size (Fig. 6g). The albite grains were weathered with densely distributed erosion pits, and sericite occurred on their surfaces (Fig. 6g). The weathering of K-feldspar and plagioclase-TIMA was also observed with some pits and unclassified minerals (speculated to be a mixture of clay minerals) on their surfaces (Fig. 6g). Biotite and chlorite were rarely observed in sample SW1, whereas the clay mineral content significantly increased (Fig. 6g). K was mainly found in K-feldspar, sericite, and clay minerals (Fig. 6h). Fe and Mg were mainly distributed in clay minerals in the weathered sample (Fig. 6i–j).

Results of the two water–rock interaction experiments

In the cyclic water–rock interaction experiment, the pH values decreased slightly and showed alkaline characteristics. However, the EC values increased steadily from 7 μs/cm to 119 μs/cm, and the TDS values increased from 3 mg/L to 59 mg/L (Fig. 7a). The concentration of ions was in the order $Ca^{2+} > Mg^{2+} > Na^{+} \approx K^{+} \approx SO_4^{2-}$. The concentration of Ca^{2+} increased steadily from 20.9 mg/L to 157.4 mg/L (Fig. 7a). The concentration of Mg^{2+} increased slowly from 2.1 mg/L to 28.3 mg/L. The concentrations of Na^+, K^+, and SO_4^{2-} were in the range of 0–2.1 mg/L and showed little variation in this experiment (Fig. 7a).

In the acid-accelerated weathering experiment, three stages were observed (Fig. 7b). In Stage I (cycles 1–18), the EC, TDS, and ionic concentrations for each cycle showed clear decreasing tendencies. The pH values showed slight alkaline characteristics, with a range of 7.04–7.84. The Ca^{2+} concentration was the highest, followed by the Mg^{2+} concentration, and the Na^+, K^+, and SO_4^{2-} concentrations were the lowest (Fig. 7b). The Ca^{2+} and Mg^{2+} concentrations were highest in the first cycle at 123.9 mg/L and 21.3 mg/L, respectively, and then presented decreasing trends. In Stage II (cycles 19–51), the EC and TDS values remained steady, with ranges of 62–101 μs/cm and 31–50 mg/L, respectively, which were much lower than those in Stage I. The pH values presented neutral characteristics in Stage II. The Ca^{2+} concentration showed a slight decreasing trend from 52.2 mg/L to 8.8 mg/L. The Na^+, K^+, and SO_4^{2-} concentrations were below 4.0 mg/L and showed little variation (Fig. 7b). In Stage III (cycles 52–67), the EC and TDS values presented large fluctuations. The pH values fluctuated between 3 and 4, showing acidic characteristics. The Ca^{2+} concentrations were in the range of 8.2–8.8 mg/L. The Mg^{2+}, Na^+, K^+, and SO_4^{2-} concentrations were below 1.0 mg/L (Fig. 7b).

Discussion

Hydrochemical characteristics of groundwater

The Piper diagram was utilized to identify the hydrochemical groundwater types. The rainwater sample R1 showed much lower ion concentrations than those in the groundwater samples (Fig. S2). The hydrochemical differences between the groundwater samples collected from different formations were not obvious (Fig. S2), which can be attributed to the similar lithologies of the Bailong and Cangxi Formations. All groundwater samples and rainwater sample from the Nankan mountainside are in the HCO_3-Ca zone (Fig. S2), which corresponds to the highest concentrations of Ca^{2+} and HCO_3^- (Table 2). The HCO_3-Ca dominance of all the samples suggests that water–rock interaction is the prevalent hydrochemical process driving groundwater chemical composition (Adimalla et al. 2020a, b; Zhang et al. 2021).

The Gibbs diagram is an efficient method for distinguishing the natural processes in groundwater chemistry, which includes three natural mechanisms: evaporation, water–rock interaction, and atmospheric precipitation (Gibbs 1970). Here, the ion ratios of $Na^+/(Na^+ + Ca^{2+})$ of groundwater samples were in the range of 0.09–0.22, which showed a small difference. The ion ratios of $Cl^-/(Cl^- + HCO_3^-)$ of groundwater samples were in the range of 0.04–0.21 (Fig. S3). Moreover, samples G3 and G6 showed the two lowest ratios of $Cl^-/(Cl^- + HCO_3^-)$, which can be attributed to their lowest Cl^- concentrations. Sample G4 showed the highest ratio of $Cl^-/(Cl^- + HCO_3^-)$ compared to the other samples, which can be attributed to its highest Cl^- concentration (Table 2). Sample G4 was near a residential area and

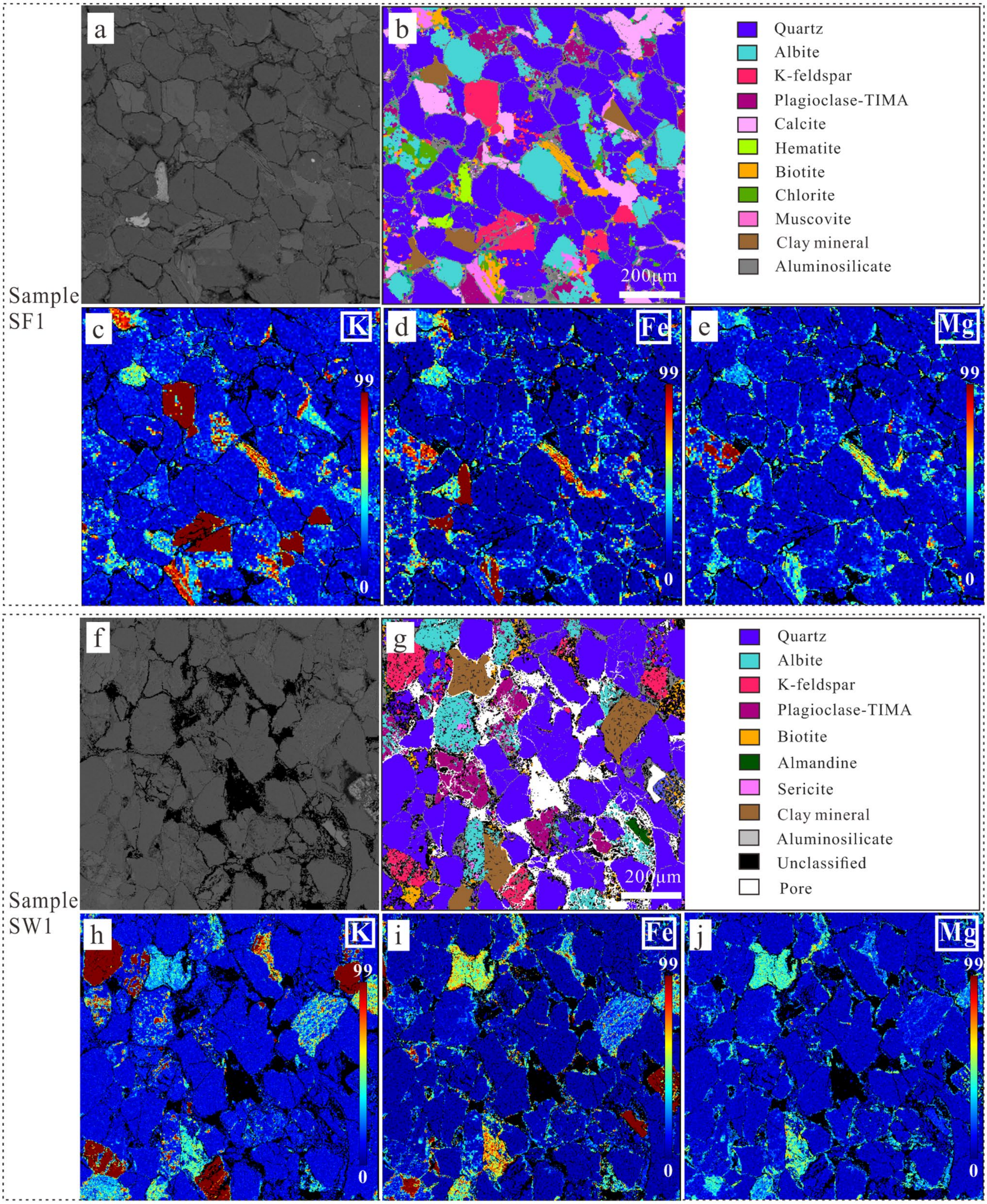

Fig. 6 BSE micrograph, mineral map, and element maps of fresh sample SF1 and weathered sample SW1. **a** BSE image of sample SF1. **b** Mineral map of sample SF1. **c–e** Element maps of sample SF1. **f** BSE image of sample SW1. **g** Mineral map of sample SW1. **h–j** Element maps of sample SW1

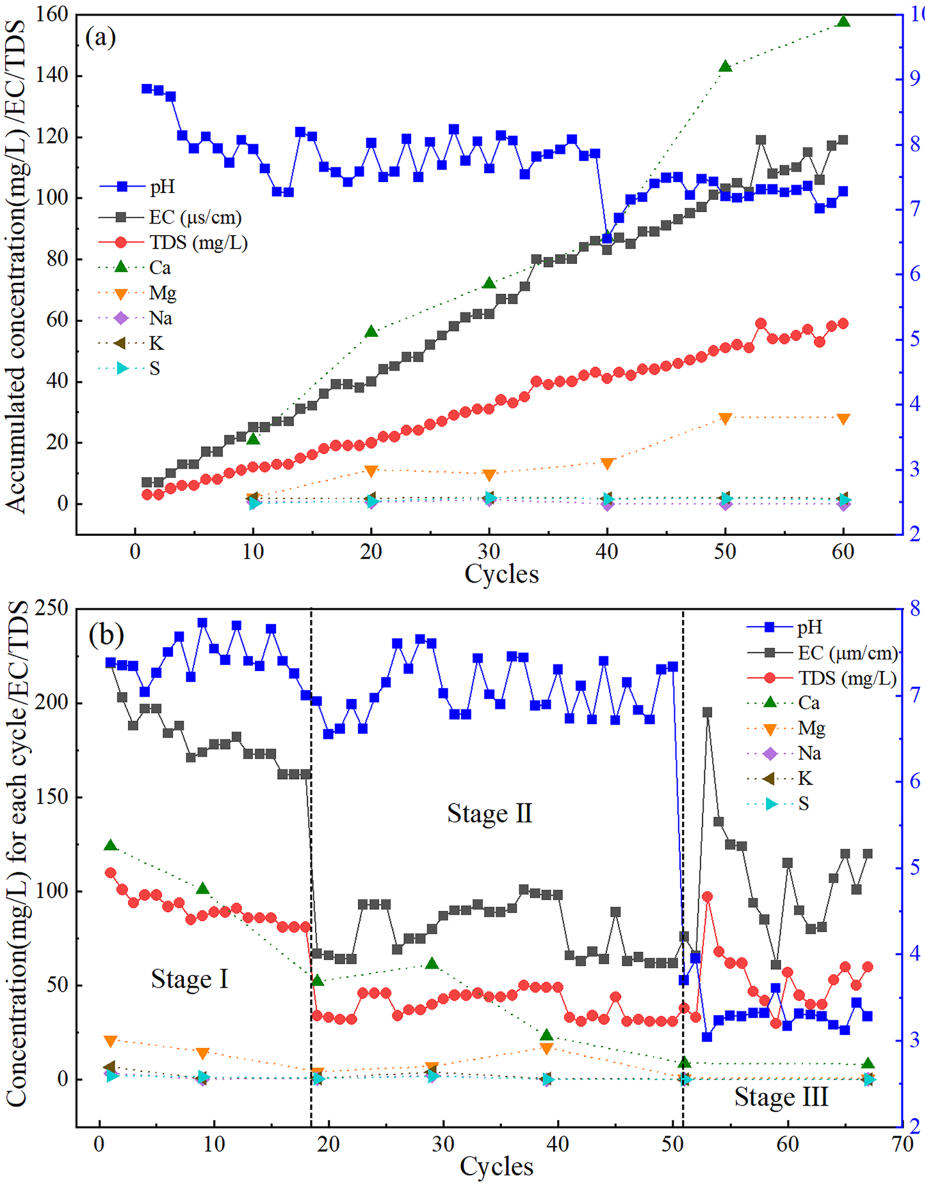

Fig. 7 pH, EC, TDS values and ionic concentrations of the two water–rock interaction experiments. **a** Cyclic water–rock interaction experiment. **b** Acid-accelerated weathering experiment

may be contaminated by domestic sewage, resulting in its highest NO_3^-, Cl^-, and K^+ concentrations. All the groundwater samples are distributed in the rock dominance area, indicating that water–rock interactions controlled the hydrochemistry of the Nankan groundwater system.

The correlations of major ions are analysed to clarify the mineral contributions to the water–rock interactions (Adimalla et al. 2020a). The ion ratios of Mg^{2+}/Na^+, Ca^{2+}/Na^+, and HCO_3^-/Na^+ are effective indices for the rock types that interacted with water (Gaillardet et al. 1999). The field groundwater samples from the Nankan mountainside are distributed in the transition area between silicate rocks and carbonate rocks (Fig. 8a, b), indicating that the groundwater chemical compositions were derived from the dissolution of carbonate and silicate minerals in the sandstone, such as calcite, albite, and plagioclase-TIMA. The ratios of (Mg^{2+}/Na^+) versus (Ca^{2+}/Na^+) and (HCO_3^-/Na^+) versus (Ca^{2+}/Na^+) are far from those observed in areas with evaporitic rocks, which is consistent with the lack of evaporites and salt rocks in the Nankan area (Table 3). The y = x line in the ($Ca^{2+} + Mg^{2+}$) versus ($HCO_3^- + SO_4^{2-}$) and Na^+ versus Cl^-diagrams suggests that the dissolution of carbonate, sulfate, and halite minerals was the main source of the chemical composition of the groundwater. The groundwater samples in the Nankan mountainside plot beyond the y = x line (Fig. 8c, d), indicating that the excess Na^+, Ca^{2+}, and Mg^{2+} concentrations were derived from the dissolution of albite and plagioclase-TIMA. The cation exchange process was verified by the chloro-alkaline indices CAI-I ($=(Cl^- - (Na^+ + K^+))/Cl^-$) and CAI-II ($=(Cl^- - (Na^+ + K^+))/(HCO_3^- + SO_4^{2-}$

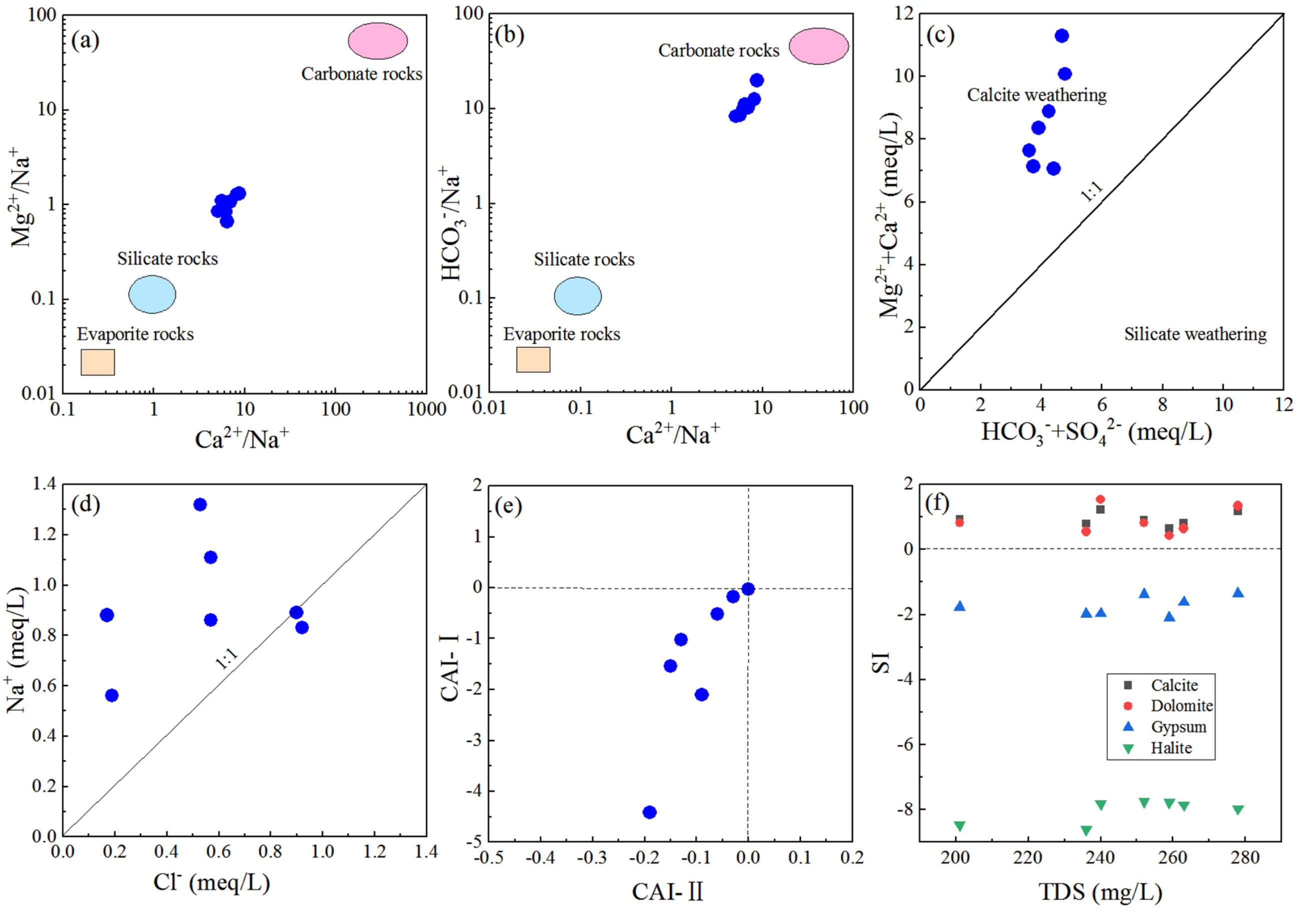

Fig. 8 Correlation diagrams of **a** (Mg^{2+}/Na^{+}) vs. (Ca^{2+}/Na^{+}), **b** (HCO_3^{-}/Na^{+}) vs. (Ca^{2+}/Na^{+}), **c** ($Ca^{2+} + Mg^{2+}$) vs. ($HCO_3^{-} + SO_4^{2-}$), **d** Na^{+} vs. Cl^{-}, **e** chloro-alkaline indices CAI-I vs. CAI-II, and **f** SI vs. TDS

$+ CO_3^{2-} + NO_3^{-}$)), which can indicate the type and intensity of cation exchange. The CAI-I and CAI-II values of the Nankan groundwater samples are mostly less than zero, suggesting that Mg^{2+} and Ca^{2+} in the groundwater replaced Na^{+} and K^{+} in the minerals (Fig. 8e) (Gao et al. 2020; Liu et al. 2021). The saturation index (SI) represents the equilibrium status of the minerals in the groundwater system and is calculated as follows (Zhang et al. 2021):

$$SI = \log \frac{IAP}{K_{sp}} \qquad (2)$$

where IAP is the ion activity product, that is, the product of the anion and cation activity of a mineral in an aqueous solution, and Ksp is the solubility product constant. The SI values of calcite and dolomite are higher than zero in the Nankan groundwater system, suggesting that calcite and dolomite reached an oversaturated status and had precipitation tendencies (Fig. 8f). However, the SI values of gypsum and halite are far lower than zero, indicating that they are in an unsaturated state and show tendencies for continuous dissolution (Fig. 8f).

Insight into microscopic weathering behaviour of primary minerals in the Nankan area

The dissolution of calcite was clearly presented in the mineral maps of the fresh and weathered rock samples (Fig. 6b, g). Abundant quantities of Ca^{2+} and HCO_3^{-} were discharged from the calcite and calcareous cement to the solution, which is in accordance with the hydrochemical HCO_3-Ca type background of the Nankan groundwater system (Fig. S2). In addition, calcite has reached the oversaturated status in the Nankan groundwater system (Fig. 8f), which also supports the dissolution of calcite from the sandstone. Therefore, calcite dissolution, as shown below (Eq. 3), was the primary hydrochemical process driving the groundwater chemical compositions.

$$CaCO_3 + H^{+} \rightarrow Ca^{2+} + HCO_3^{-} \qquad (3)$$

The concentration of Mg^{2+} in the solution of cyclic water–rock interaction experiment also showed an increasing trend (Fig. 7a). Mg was mainly concentrated in chlorite and biotite in the fresh sample SF1, as evidenced by its elemental map (Fig. 6e). Mg^{2+} was verified to be released during the weathering of biotite and the weathering of chlorite-(Mg) (Buss et al. 2008; Murphy et al. 1998). Therefore, the processes of biotite alteration to chlorite-(Mg) and the weathering of chlorite-(Mg) were the main sources of Mg^{2+} in the Nankan groundwater system. The weathering of biotite in the Nankan Grotto is described by Eq. (4), and the weathering of chlorite-(Mg) in the Nankan Grotto is described by Eq. (5). The primary mineral formulas of sandstone in the Nankan Grotto was calculated by EDS elemental composition analysis (with the TIMA) based on the stated oxygen number (Behrens et al. 2021).

$$\begin{gathered}10K_{0.9}(Fe_{1.4}Mg_{0.9}Ti_{0.2})(Al_{1.6}Si_{2.9})O_{10}(OH)_2\\ + 22.4H^+ + 20.8H_2O \rightarrow 8Al_2Si_2O_5(OH)_4 + 13H_4SiO_4\\ + 9K^+ + 9Mg^{2+} + 5.6(Fe_{2.5}Ti_{0.2})O_3 + 0.88Ti^{4+}\end{gathered} \tag{4}$$

$$\begin{gathered}2(Fe_{0.9}Mg_{4.2})(Al_{2.6}Si_{4.5})O_{10}(OH)_8 + 2.6H^+\\ +5.6H_2O \rightarrow 2Al_2Si_2O_5(OH)_4 + 5H_4SiO_4\\ +8.4Mg^{2+} + 1.8FeO(OH) + 1.2Al^{3+}\end{gathered} \tag{5}$$

Sericite and other lamellar clay minerals were observed on the surfaces of albite and plagioclase-TIMA (Fig. 5i, j; Fig. 6g). During the weathering process of albite and plagioclase-TIMA alteration to clay minerals, Na^+ and Ca^{2+} could be released into the solution (Brantley et al. 2007; Ji et al. 2004; Wei et al. 2021; White et al. 1998). Therefore, Na^+ in the Nankan groundwater system was due to the weathering of albite and plagioclase-TIMA. The weathering of plagioclase-TIMA was also an additional supplement of Ca^{2+}. The weathering of albite in the Nankan area is described by Eq. (6) and the weathering of plagioclase-TIMA in the Nankan area is described by Eq. (7).

$$\begin{gathered}10Na_{1.2}Al_{1.0}Si_{2.9}O_8 + 14H^+ + 41H_2O\\ \rightarrow 5Al_2Si_2O_5(OH)_4 + 19H_4SiO_4 + 12Na^+\end{gathered} \tag{6}$$

$$\begin{gathered}10(Na_{0.8}Ca_{0.2})Al_{1.3}Si_{2.7}O_8 + 16H^+ + 34H_2O\\ \rightarrow 6Al_2Si_2O_5(OH)_4 + 15H_4SiO_4 + 2Ca^{2+} + 8Na^+ + Al^{3+}\end{gathered} \tag{7}$$

During the process of biotite alteration to chlorite-(Mg), K was depleted from biotite (Dong et al. 1998; Murphy et al. 1998). Therefore, the weathering of biotite released K^+ into the solution (Eq. 4). In addition, the slight weathering of K-feldspar released minor amounts of K^+ into the solution in the Nankan groundwater system (Eq. 8).

$$\begin{gathered}2K_{0.8}Al_{1.1}Si_3O_8 + 2H^+ + 9H_2O\\ \rightarrow Al_2Si_2O_5(OH)_4 + 4H_4SiO_4 + 1.6\,K^+ + 0.2Al^{3+}\end{gathered} \tag{8}$$

Deterioration mechanism of the Nankan sandstone heritage site

In the cyclic water–rock interaction experiment, the concentration of Ca^{2+} increased sharply, the concentration of Mg^{2+} increased more slowly with increasing interaction time, and these ions were the dominant contributors to the increases in EC and TDS (Fig. 7a). The Ca^{2+} and Mg^{2+} dominance of the interacting solution was consistent with the field Nankan groundwater characteristics (Table 2). These results suggest that the major reaction was calcite dissolution in the cyclic water–rock interaction experiment, while feldspar dissolution was minor. Therefore, an acid-accelerated weathering experiment was necessary to explore all possible processes of sandstone weathering. In the acid-accelerated weathering experiment, three weathering stages could be classified: calcite dissolution stage (Stage I), feldspar weathering stage (Stage II), and faint–weathering stage (Stage III) (Fig. 7b). In Stage I, calcite was preferentially weathered (corresponding to Fig. 9a, b). This stage released bulk Ca^{2+} into the interacting solution, which contributed to the high EC and TDS values. The H^+ in the added solution was completely consumed in the interaction with calcite in each cycle, so the pH values showed slight alkaline characteristics (Fig. 7b). At the end of Stage I, the calcite was completely dissolved from the sandstone powder (Fig. 9b). In Stage II, the weathering of feldspar was dominant (corresponding to Fig. 9c, d). Because feldspar had a lower weathering rate, it released fewer ions into the interacting solution, which led to lower EC and TDS values in Stage II. The pH values presented neutral characteristics, suggesting that the H^+ in the added solution was also completely consumed in Stage II (Fig. 7b). In Stage III, almost no reaction occurred (Fig. 7b), as demonstrated by the pH values of the interacting solution being close to the pH of the original added HNO_3 solution ($pH = 3$).

In general, the deterioration of sandstone can be attributed to the weathering of primary minerals. Calcite was the most vulnerable to the acid solution during the weathering process (Fig. 9a–b), which was supported by the complete depletion of calcite in the mineral map (Fig. 6g) and the rapid dissolution of Ca^{2+} in the water–rock interaction experiment and acid-accelerated weathering experiment (Fig. 7). In biotite, Fe^{2+} was oxidized to ilmenite, and the residue was altered to chlorite-(Mg) (Fig. 5g). The weathering of biotite was verified to be faster than plagioclase because of the preferential oxidation of structural Fe(II) in biotite (Behrens et al. 2021). The weathering of biotite was also an important cause of sandstone deterioration in the Nankan Grotto (Fig. 9b, c), even though the concentration of biotite was very low and not detected by XRD. Moreover, sericite and other lamellar clay minerals were observed on the albite surfaces, as directly verified by the BSE images and mineral map (Figs. 5a, c

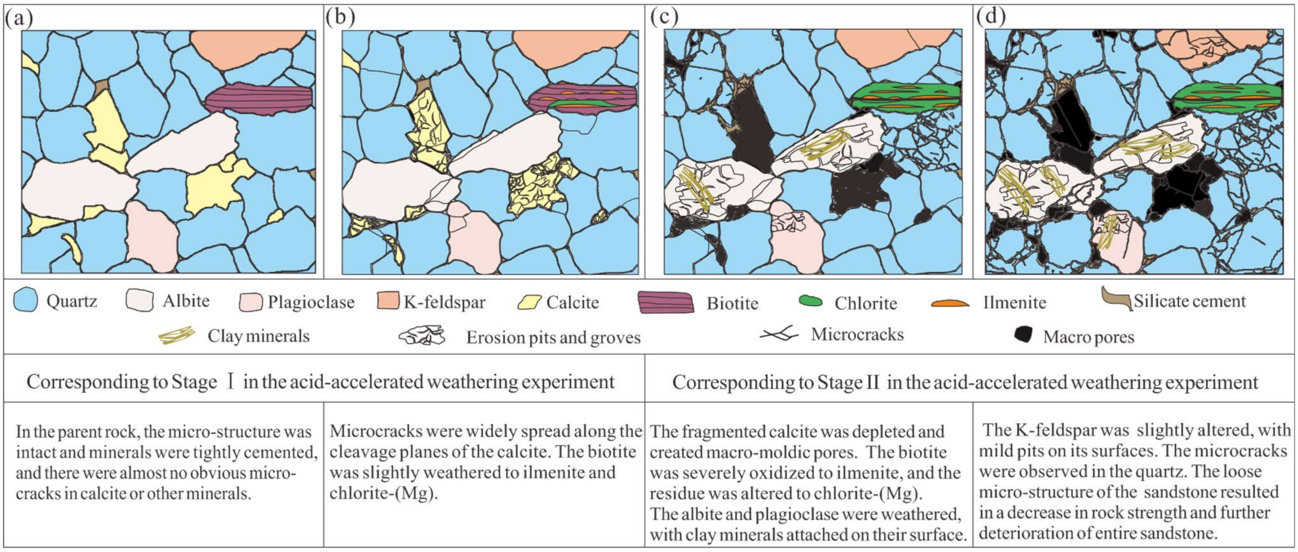

Corresponding to Stage Ⅰ in the acid-accelerated weathering experiment		Corresponding to Stage II in the acid-accelerated weathering experiment	
In the parent rock, the micro-structure was intact and minerals were tightly cemented, and there were almost no obvious micro-cracks in calcite or other minerals.	Microcracks were widely spread along the cleavage planes of the calcite. The biotite was slightly weathered to ilmenite and chlorite-(Mg).	The fragmented calcite was depleted and created macro-moldic pores. The biotite was severely oxidized to ilmenite, and the residue was altered to chlorite-(Mg). The albite and plagioclase were weathered, with clay minerals attached on their surface.	The K-feldspar was slightly altered, with mild pits on its surfaces. The microcracks were observed in the quartz. The loose micro-structure of the sandstone resulted in a decrease in rock strength and further deterioration of entire sandstone.

Fig. 9 Schematic diagram of the microweathering processes of the minerals in the Nankan Grotto sandstone

and 6g). Clay minerals were also observed in the plagioclase-TIMA (Figs. 5i, j and 6g). However, the degree of K-feldspar weathering was slight (Figs. 5 and 6), as evidenced by the lowest concentration of K^+ in the Nankan groundwater system (Table 2). The weathering of plagioclase-TIMA and albite to clay minerals occurred prior to that of K-feldspar (Ji et al. 2004; Middelburg et al. 1988; White et al. 1996). Consequently, the acid solution attacked the primary minerals in the Nankan Grotto sandstone, promoting their alteration to secondary minerals. The main processes included the dissolution of calcite, the weathering of biotite to ilmenite and chlorite-(Mg), and the alteration of albite and plagioclase-TIMA to clay minerals. These processes created microcracks in the mineral grains and generated macrocracks or pores between the minerals (Fig. 9d), leading to the poor cementation of the minerals (Ling et al. 2018; Molenaar et al. 2021). The loose microstructure of the sandstone resulted in a decrease in rock strength and a further deterioration of the sandstone in the Nankan Grotto.

Conclusions

The hydrochemical characteristics of the groundwater were investigated and micro-observations were undertaken for the sandstone in the Nankan Grotto. In addition, two water–rock interaction experiments were designed. The main conclusions can be summarized as follows.

1. The groundwater samples around Nankan Mountain displayed HCO_3-Ca dominance, which was mainly derived from the dissolution of carbonate and silicate minerals. Combined with the microscopic petrographical analyses for solid sandstone samples, we can draw the following conclusions: Ca^{2+} was mainly discharged by the weathering of calcite, and minor amounts of Ca^{2+} were released from the weathering of plagioclase-TIMA. Mg^{2+} was discharged by the weathering of biotite and chlorite-(Mg). Na^+ was released by the alteration of albite and plagioclase-TIMA to clay minerals. K^+ was released by the weathering of K-feldspar and biotite.
2. The two water–rock interaction experiments and the microscopic observations for minerals demonstrated the weathering sequence for the minerals in the Nankan Grotto sandstone. The deterioration mechanism of sandstone can be attributed to the weathering of primary minerals. The main processes included the dissolution of calcite, the weathering of biotite to ilmenite and chlorite-(Mg), and the alteration of albite and plagioclase-TIMA to clay minerals.
3. The abovementioned mineral weathering processes led to poor cementation of the microstructure and to further deterioration of the sandstone in the Nankan Grotto. The three methodologies, that is, field water analysis, microscopic observations for sandstone, and water−rock interaction experiments, provided compelling evidence and complemented each other, thereby synergistically clarifying the deterioration mechanisms of sandstone

caused by water–rock interactions in the Nankan Grotto. In addition to the conclusions being evident and universal, they pave the way for the subsequent conservation of the Nankan Grotto. The research methodology in this study can also be applied to research and conservation of other sandstone heritage sites.

Supplementary Information The online version contains supplementary material available at https://doi.org/10.1007/s10064-023-03378-y.

Acknowledgements We greatly appreciate the colleagues of Nankan Grotto Research Institute for their supports in the field investigations. We also thank the colleagues of Nanjing Hongchuang Geological Exploration Technology Service Co., Ltd. of China for their helps in sample texting. This study was funded by the National Natural Science Foundation of China (No. 42077271, 41877215), Sichuan Science and Technology Program (No. 2023YFS0364), Chengdu Science and Technology Program (2022-YF05-00240-SN). Additionally, Xuening Zhang also thanks her husband Yi Yu for his inspiration.

Data Availability All the data has displayed in the manuscript. If you need the original data, please contact with authors.

Declarations

Competing interest The authors declare that they have no known competing financial interests or personal relationships that could have appeared to influence the work reported in this paper.

References

Adimalla N, Qian H, Li P (2020a) Entropy water quality index and probabilistic health risk assessment from geochemistry of groundwaters in hard rock terrain of Nanganur County, South India. Geochemistry 80:125544. https://doi.org/10.1016/j.chemer.2019.125544

Adimalla N, Qian H, Nandan MJ (2020b) Groundwater chemistry integrating the pollution index of groundwater and evaluation of potential human health risk: A case study from hard rock terrain of south India. Ecotoxicol Environ Saf 206:111217. https://doi.org/10.1016/j.ecoenv.2020.111217

André M-F, Voldoire O, Roussel E, Vautier F, Phalip B, Peou H (2012) Contrasting weathering and climate regimes in forested and cleared sandstone temples of the Angkor region. Earth Surf Proc Land 37:519–532. https://doi.org/10.1002/esp.2265

Behrens R, Wirth R, Blanckenburg FV (2021) Rate limitations of nanoscale weathering front advance in the slow-eroding Sri Lankan Highlands. Geochim Cosmochim Acta 311:174–197. https://doi.org/10.1016/j.gca.2021.06.003

Bonomo AE, Amodio AM, Prosser G, Sileo M, Rizzo G (2020) Evaluation of soft limestone degradation in the Sassi UNESCO site (Matera, Southern Italy): Loss of material measurement and classification. J Cult Herit 42:191–201. https://doi.org/10.1016/j.culher.2019.07.017

Brantley SL, Goldhaber MB, Ragnarsdottir KV (2007) Crossing disciplines and scales to understand the critical zone. Elements 3(5):307–314. https://doi.org/10.2113/gselements.3.5.307

Buss HL, Sak PB, Webb SM, Brantley SL (2008) Weathering of the Rio Blanco quartz diorite, Luquillo Mountains, Puerto Rico: Coupling oxidation, dissolution, and fracturing. Geochim Cosmochim Acta 72:4488–4507. https://doi.org/10.1016/j.gca.2008.06.020

Cardell C, Delalieux F, Roumpopoulos K, Moropoulou A, Auger F, Van Grieken R (2003) Salt-induced decay in calcareous stone monuments and buildings in a marine environment in SW France. Constr Build Mater 17:165–179. https://doi.org/10.1016/s0950-0618(02)00104-6

Dong HL, Peacor DR, Murphy SF (1998) TEM study of progressive alteration of igneous biotite to kaolinite throughout a weathered soil profile. Geochim Cosmochim Acta 62(11):1881–1887. https://doi.org/10.1016/s0016-7037(98)00096-9

Dursun F, Topal T (2019) Durability assessment of the basalts used in the Diyarbakır City Walls, Turkey. Environ Earth Sci 78:456. https://doi.org/10.1007/s12665-019-8466-y

Gaillardet J, Dupré B, Louvat P, Allègre CJ (1999) Global silicate weathering and CO_2 consumption rates deduced from the chemistry of large rivers. Chem Geol 159:3–30. https://doi.org/10.1016/s0009-2541(99)00031-5

Gao Y, Qian H, Ren W, Wang H, Liu F, Yang F (2020) Hydrogeochemical characterization and quality assessment of groundwater based on integrated-weight water quality index in a concentrated urban area. J Clean Prod 260:121006. https://doi.org/10.1016/j.jclepro.2020.121006

Germinario L, Oguchi CT (2022) Gypsum, mirabilite, and thenardite efflorescences of tuff stone in the underground environment. Environ Earth Sci 81:242. https://doi.org/10.1007/s12665-022-10344-6.10.1007/s12665-022-10344-6

Germinario L, Oguchi CT, Tamura Y, Ahn S, Ogawa M (2020) Taya Caves, a Buddhist marvel hidden in underground Japan: stone properties, deterioration, and environmental setting. Herit Sci 8:87. https://doi.org/10.1186/s40494-020-00433-9

Gibbs RJ (1970) Mechanisms controlling world water chemistry. Science 170:1088–1090. https://doi.org/10.1126/science.170.3962.1088

Grøntoft T, Cassar J (2020) An assessment of the contribution of air pollution to the weathering of limestone heritage in Malta. Environ Earth Sci 79:288. https://doi.org/10.1007/s12665-020-09027-x

Hatır ME, Korkanç M, Başar ME (2018) Evaluating the deterioration effects of building stones using NDT: the Küçükköy Church, Cappadocia Region, central Turkey. Bull Eng Geol Env 78:3465–3478. https://doi.org/10.1007/s10064-018-1339-x

Hosono T, Uchida E, Suda C, Ueno A, Nakagawa T (2006) Salt weathering of sandstone at the Angkor monuments, Cambodia: identification of the origins of salts using sulfur and strontium isotopes. J Archaeol Sci 33:1541–1551. https://doi.org/10.1016/j.watres.2013.02.020

Ji HB, Wang SB, Ouyang ZY, Zhang S, Sun CX, Liu XM, Zhou DQ (2004) Geochemistry of red residua underlying dolomites in karst terrains of Yunnan-Guizhou Plateau: I. The formation of the Pingba profile. Chem Geol 203:1–27. https://doi.org/10.1016/j.chemgeo.2003.08.012

Levett A, Vasconcelos PM, Gagen EJ, Rintoul L, Spier C, Guagliardo P, Southam G (2020) Microbial weathering signatures in lateritic ferruginous duricrusts. Earth Planet Sci Lett 538:116209. https://doi.org/10.1016/j.epsl.2020.116209

Ling SX, Wu XY, Zhao SY, Liao X (2018) Evolution of porosity and clay mineralogy associated with chemical weathering of black shale: A case study of Lower Cambrian black shale in Chongqing, China. J Geochem Explor 188:326–339. https://doi.org/10.1016/j.gexplo.2018.02.002

Liu JT, Peng YM, Li CS, Gao ZJ, Chen SJ (2021) Characterization of the hydrochemistry of water resources of the Weibei Plain, Northern China, as well as an assessment of the risk of high groundwater nitrate levels to human health. Environ Pollut 268:115947. https://doi.org/10.1016/j.envpol.2020.115947

Liu XB, Koestler RJ, Warscheid T, Katayama Y, Gu JD (2020) Microbial deterioration and sustainable conservation of stone monuments and buildings. Nat Sustain 3:991–1004. https://doi.org/10.1038/s41893-020-00602-5

Middelburg JJ, van der Weijden CH, Woittiez JRW (1988) Chemical processes affecting the mobility of major, minor and trace elements during weathering of granitic rocks. Chem Geol 68:253–273. https://doi.org/10.1016/0009-2541(88)90025-3

Molenaar N, Vaznytė J, Bär K, Šliaupa S (2021) Illite and chlorite cementation of siliciclastic sandstones influenced by clay grain cutans. Mar Pet Geol 132:105234. https://doi.org/10.1016/j.marpetgeo.2021.105234

Murphy SF, Brantley SL, Blum AE, White AF, Dong H (1998) Chemical weathering in a tropical watershed, Luquillo Mountains, Puerto Rico: II. Rate and mechanism of biotite weathering. Geochim Cosmochim Acta 62(2):227–243. https://doi.org/10.1016/S0016-7037(97)00336-0

Paradise TR (1995) Sandstone Weathering Thresholds in Petra, Jordan. Phys Geogr 16:205–222. https://doi.org/10.1080/02723646.1995.10642550

Rothert E, Eggers T, Cassar J, Ruedrich J, Fitzner B, Siegesmund S (2007) Stone properties and weathering induced by salt crystallization of Maltese Globigerina Limestone. Geological Society, London, Special Publications 271:189–198. https://doi.org/10.1144/gsl.sp.2007.271.01.19

Ruedrich J, Siegesmund S (2007) Salt and ice crystallisation in porous sandstones. Environ Geol 52:225–249. https://doi.org/10.1007/s00254-006-0585-6

Sabbioni C, Zappia G (1992) Decay of sandstone in urban areas correlated with atmospheric aerosol. Water Air Soil Pollut 63:305–316. https://doi.org/10.1007/bf00475497

Siedel H (2018) Salt efflorescence as indicator for sources of damaging salts on historic buildings and monuments: a statistical approach. Environ Earth Sci 77:1–20. https://doi.org/10.1007/s12665-018-7752-4

Siegesmund S, Snethlage S (2011) Stone in Architecture: Properties, Durability. Springer Science & Business Media

Sun CW, Ling SX, Wu XY, Li XN, Chen JN, Jiang WC (2021) Oxidation of black shale and its deterioration mechanism in the slip zone of the Xujiaping landslide in Sichuan Province, Southwestern China. Catena 200:105139. https://doi.org/10.1016/j.catena.2020.105139

Sun Q, Zhang Y (2019) Combined effects of salt, cyclic wetting and drying cycles on the physical and mechanical properties of sandstone. Eng Geol 248:70–79. https://doi.org/10.1016/j.enggeo.2018.11.009

Wei W, Ling SX, Wu XY, Li XN, Liao X (2021) Investigations on mineralogy and geochemistry of a black shale profile on the northern Yangtze platform, China: Weathering fate of rare earth elements and yttrium (REY) and its implications. Appl Geochem 126:104897. https://doi.org/10.1016/j.apgeochem.2021.104897

White AF, Blum AE, Schulz MS, Bullen TD, Harden JW, Peterson ML (1996) Chemical weathering rates of a soil chronosequence on granitic alluvium: I. Quantification of mineralogical and surface area changes and calculation of primary silicate reaction rates. Geochim Cosmochim Acta 60(14):2533–2550. https://doi.org/10.1016/0016-7037(96)00106-8

White AF, Blum AE, Schulz MS, Vivit DV, Eberl D (1998) Chemical weathering in a tropical watershed, Luquillo Mountains, Puerto Rico: I. Long-term versus short-term weathering fluxes. Geochim Cosmochim Acta 62(2):209–226. https://doi.org/10.1016/S0016-7037(97)00335-9

Williams RBG, Robinson DA (2000) Effects of aspect on weathering: anomalous behaviour of sandstone gravestones in southeast England. Earth Surf Proc Land 25(2):135–144. https://doi.org/10.1002/(sici)1096-9837(200002)25:2%3c135::aid-esp50%3e3.0.co;2-9

Xu HB, Tsukuda M, Takahara Y, Sato T, Gu JD, Katayama Y (2018) Lithoautotrophical oxidation of elemental sulfur by fungi including Fusarium solani isolated from sandstone Angkor temples. Int Biodeterior Biodegradation 126:95–102. https://doi.org/10.1016/j.ibiod.2017.10.005

Yan SJ, Xie N, Liu JH, Li L, Peng LZ, Jiang SW (2022) Salt weathering of sandstone under dehydration and moisture absorption cycles: An experimental study on the sandstone from Dazu rock carvings. Earth Surf Proc Land 47:977–993. https://doi.org/10.1002/esp.5298

Yu S, Oguchi CT (2010) Role of pore size distribution in salt uptake, damage, and predicting salt susceptibility of eight types of Japanese building stones. Eng Geol 115:226–236. https://doi.org/10.1016/j.enggeo.2009.05.007

Zammit T, Cassar J (2015) Investigating possible correlations between the porosimetry and insoluble residue content of Malta's Lower Globigerina Limestone. Bull Eng Geol Env 76:59–70. https://doi.org/10.1007/s10064-015-0817-7

Zhang YH, Dai YS, Wang Y, Huang X, Xiao Y, Pei QM (2021) Hydrochemistry, quality and potential health risk appraisal of nitrate enriched groundwater in the Nanchong area, southwestern China. Sci Total Environ 784:147186. https://doi.org/10.1016/j.scitotenv.2021.147186